Influence of novel anode design on the performance and coke resistance towards methane directly-fed solid oxide fuel cells

Sarruf, Bernardo; Hong, Jong-Eun; Steinberger-Wilckens, Robert; de Miranda, Paulo Emilio V.

DOI:
10.1016/j.ceramint.2019.10.292

Document Version
Peer reviewed version

Citation for published version (Harvard):
Sarruf, B, Hong, J-E, Steinberger-Wilckens, R & de Miranda, PEV 2020, 'Influence of novel anode design on the performance and coke resistance towards methane directly-fed solid oxide fuel cells', *Ceramics International*, vol. 46, no. 4, pp. 5368-5379. https://doi.org/10.1016/j.ceramint.2019.10.292

Influence of novel anode design on the performance and coke resistance towards methane directly-fed solid oxide fuel cells

Bernardo Jordão Moreira Sarruf[a*], Jong-Eun Hong[b*],
Robert Steinberger-Wilckens[c], Paulo Emílio Valadão de Miranda[a]

[a]*Hydrogen Laboratory COPPE Metallurgical and Materials Engineering, Federal University of Rio de Janeiro, - Rio de Janeiro, Brazil – 21942-971b*
[b]*Fuel Cell Laboratory, Korea Institute of Energy Research 152, Gajeong-ro, Yuseong-gu, Daejeon, South Korea – 34129*
[c]*Centre for Fuel Cell and Hydrogen Research, School of Chemical Engineering, University of Birmingham, Edgbaston, Birmingham, UK – B152TT*

Abstract

The direct utilisation of primary fuels such as natural gas, green methane or ethanol represents a transition step towards a cleaner energy-based society. This work shows the influence of a nickel-free intermediate anode layer, and a ceria-based functional anode composite, on solid oxide fuel cell (SOFC) performance when directly utilising dry methane without fuel pre-reforming. A CeO_2-Co_3O_4-CuO electrocatalyst was investigated by X-ray diffraction and X-ray fluorescence to confirm the presence of CeO_2, Co_3O_4, and CuO phases. To avoid thermal mismatches between the anode/electrolyte, an anode intermediate layer was developed and tested, with the aim of enhancing the thermal and chemical compatibility of components and oxygen ion transfer within the anode. The electrochemical properties of the assembled cells were evaluated by measuring i-V plots and electrochemical impedance spectra. The addition of the intermediate layer substantially decreased the polarisation resistance of the cell and increased the electrochemical performance of the cell 2.5- to 5.5-fold depending on which fuel was being utilised. Scanning electron microscopy was performed to observe the integrity of the microstructure morphology of both anode assemblies. The utilisation of dry methane was shown to be viable for operation from 750 to 850˚C within the developed cells. Furthermore, Raman spectroscopy and temperature-programmed oxidation tests confirmed that carbon deposition over the anode surface was negligible within the proposed configuration and materials design. Accordingly, this study reveals that the addition of the intermediate layer is promising for improving SOFC performance and mitigating carbon coking under direct methane-fuelled operation.

Keywords*:* Solid oxide fuel cells, anode intermediate layer, coke-resistant anode, dry methane as fuel

*Corresponding authors Email address:

jehong@kier.re.kr (Jong-Eun Hong), sarruf@labh2.coppe.ufrj.br (B.J.M. Sarruf)

Preprint submitted to Ceramics International September 20, 2019

1. Introduction

Much effort has been made to seek suitable materials for solid oxide fuel cells (SOFCs) capable of operating at lower temperatures and exploiting primary fuels such as hydrocarbons or alcohols. For this, a variety of issues must be taken into account. Although nickel-based materials have been explored targeting methane reforming [1, 2], in the case of methane directly-fed SOFCs, carbon deposition causes anode deactivation, and sulphur poisons conventional nickel-based anode materials [3]. It is well known that reactions such as methane cracking, carbon monoxide reduction, or the Boudouard reaction are pathways that should be avoided in these cases.

Furthermore, the strategies for utilising hydrocarbons as fuels within nickel-based anodes are mainly focused on the reaction process in which the fuels are fed with an oxidising agent such as water or carbon dioxide [4-8]. The oxidising agent promotes fuel reforming within the anode (internal reforming) and thus produces a hydrogen-rich product such as syngas of hydrogen and carbon monoxide, which can be fully oxidised within the anode, thereby avoiding undesirable carbon deposition. However, the oxidant-assisted internal reforming increases the system complexity and requires auxiliary equipment, which consequently decreases the overall efficiency of the plant and adds costs. Researchers have thus sought to develop Ni-free anode materials in recent years.

Perovskite materials and perovskite-doped materials, for instance, are being used for direct hydrocarbon utilisation with reasonable results. He *et al.* [9] were able to enhance their Sr_2NiMoO_6 by doping it with titanium, whereas Silva and Miranda [10] were able to synthesise different sorts of $LaAlO_3$ doped perovskites such as $La_{0.8}Sr_{0.2}AlO_{2.9}$, $LaAl_{0.5}Mn_{0.5}O_{2.75}$, and $La_{0.8}Sr_{0.2}Al_{0.5}Mn_{0.5}O_{2.65}$, for methane electrooxidation into C_2 hydrocarbons and power. Venâncio *et al.* [11] built on the work of [10] by showing a perovskite-based material that is able to operate with methane to co-produce power and C_2 hydrocarbons, using a SOFC as an electrochemical conversion reactor rather than just an energy converter.

Materials such as ceria-based electrocatalysts have already been identified for the direct use of hydrocarbons or ethanol with promising results. Lee *et al.* [12, 13] and Fuerte *et al.* [14] demonstrated the development of ceria-based bimetallic catalysts for utilisation of hydrocarbons as fuels. However, Lee *et al.* [12, 13] pointed out that an excess of cobalt in their Co-Cu ceria-based alloy rendered the material

prone to coke formation. On the other hand, Fuerte *et al.* [14] did not achieve good results when CH_4 was fed without any H_2 addition (e.g. pure CH_4 = 13 mW.cm^{-2} and CH_4/H_2 = 76 mW.cm^{-2}).

Furthermore, different types of ceria-based anodes have shown ability to electrooxidise hydrocarbons and alcohols. However, ceria-based materials bring a trade-off between electrical conductivity and anode stability over time when direct carbonaceous fuels are involved [14-16].

The electrochemical oxidation of hydrocarbons is able to inhibit the carbon coking whilst maintaining high efficiencies by fully oxidising the fuel. Equations 1 and 2 show the electrochemical partial and total oxidation of methane, respectively [17], which are expected to occur in the presence of oxygen ions.

$$CH_4 + O^{2-} \rightarrow CO + 2H_2 + 2e^- \qquad \Delta H = -36\, kJ.mol^{-1} \tag{1}$$

$$CH_4 + 4O^{2-} \rightarrow CO_2 + 2H_2O + 8e^- \qquad \Delta H = -802\, kJ.mol^{-1} \tag{2}$$

In Sarruf *et al.* [18, 19], the ability of our developed ceria-Co-Cu electrocatalyst to operate with direct carbonaceous fuels such as methane and ethanol was demonstrated well. However, not many works in the literature have focused on the thermal compatibility of nickel-free anodes and electrolyte materials. Therefore, as a means to add up to our previous work mentioned above, the present work studies the advantages of adding an intermediate layer between the ceria-Co-Cu anode and a zirconia-based electrolyte as a thermal mismatch mitigator.

Thermal mismatches between metallic-based anodes and ceramic electrolyte are a known problem. For instance, components such as Co_3O_4 and CuO have a coefficient of thermal expansion (CTE) of 6 × 10^{-6} K^{-1} [20] and 5 × 10^{-6} K^{-1} [21], respectively. Upon reduction, the CTEs of Co and Cu rise to 15-17 × 10^{-6} K^{-1}. However, zirconia-based ceramics are known to have thermal coefficients around 9-11 × 10^{-6} K^{-1} [22] whereas CeO_2 has a CTE of 12-14 × 10^{-6} K^{-1} [23, 24], which is closer to the electrolyte material. Therefore, a ceria/electrolyte intermediate layer was developed with the aim of impeding the thermal effects between the anode and electrolyte whilst maintaining a suitable charge transfer capacity between them.

The electrochemical path of methane oxidation is thus expected to occur, as delineated in Equations 1 and 2, which represent the less complex process of methane utilisation as fuel, provided it is additionally

possible to avoid carbon formation. The material, produced by the amorphous citrate method, is thoroughly studied in terms through the redox cycles behaviour and electrochemical impedance tests of the cells to demonstrate enhanced quality of the interface between electrolyte and anode due to the insertion of a CeO_2-ScCeSZ-based intermediate layer, which is the main novel contribution of this work. The electrochemical results are presented both for a baseline material, without the intermediate layer, and the optimised configuration with thermal mismatches issues mitigated by the presence of the intermediate layer, highlighting the differences in performance.

2. Experimental

2.1 Electrocatalyst Synthesis

The electrocatalyst powder was synthesised via the amorphous citrate method, where the precursor nitrates were $Ce(NO_3)_3.6H_2O$ by Aldrich, as well as $Co(NO_3)_2.6H_2O$ and $Cu(NO_3)_2.3H_2O$ by Sigma-Aldrich. The nitrates were dissolved in deionised water with a cerium:cobalt:copper molar ratio of 2:1:1. Saturated aqueous solutions of citric acid (Sigma-Aldrich) were then added to each nitrate solution at a molar ratio of 1:1 for each cation to citrate. The three citrate-nitrate solutions were then mixed together, and the pH was adjusted to the neutral condition (pH 7) aided by a NH_4OH solution (Fisher Scientific) at 70˚C under constant magnetic stirring. The solution was then heated to 80˚C and kept under stirring until a gel was formed. Finally, the gel was heated to 90˚C to dry. In the end, the dried product was heated to 200˚C and dwelled for 6 hours. The ashes obtained were pulverised with an agate mortar and a pestle.

2.2 Electrocatalyst characterisation

X-ray diffraction (XRD) analysis was performed using the as-synthesised electrocatalyst and a heat-treated aliquot treated in air at 800˚C for 2 hours. A Bruker D8 diffractometer was used in the range between 10 to 90˚ under radiation $Cu_{K\alpha}$ = 0.15418 nm, with 40 kV acceleration voltage and 30 mA applied current.

X-ray fluorescence (XRF) was performed in a Bruker S8 Tiger XRF Spectrometer using pelletised powder samples that were pressed with a load of two metric tons using a die of 13 mm diameter, after being mixed with wax in a mass ratio of 5:1 for powder to wax. XRF scanning was carried out using an 18-minute counting setup.

H_2-temperature-programmed reduction (H_2-TPR) and the O_2-pulse-controlled oxidation (PCO) tests were performed in two cycles to observe the redox capacity of the ceria-Co-Cu electrocatalyst. First, the H_2-TPR profile was taken from room temperature to 900˚C at 10 ˚C.min^{-1} steps. The first O_2-PCO cycle could then be done over the reduced sample at 500˚C. The O_2-PCO consisted of known injections (around 100 µL) of oxygen into the reactor until a break-through point was attained, with the aim of measuring the amount of oxygen needed to fully re-oxidise the powder aliquot that was reduced during H_2-TPR. After full oxidation, the sample was brought to room temperature and a second cycle of H_2-TPR was performed followed by a second cycle of O_2-PCO. The sample was cycled twice to observe any changes in the H_2-TPR profile due to eventual particle growth and catalyst performance.

2.3 Ceria-based intermediate layer design and cell assembly

Due to thermal mismatches between the anode and the electrolyte components, as mentioned in the introduction section, an intermediate layer was developed to prevent physical failure such as cracking or partial delamination and to increase the electro-catalytic reactivity by enlarging the effective triple phase boundaries at the interface. This intermediate layer was composed of CeO_2 and scandia-ceria stabilised zirconia (10Sc1CeZr) from Daiichi Kigenso Kagaku Kogyo mixed at a weight ratio of 1:1. For the sake of comparison, a baseline cell (with no intermediate layer) was produced. The intermediate layer powder mixture was also submitted to XRD analysis from 20 to 80˚ with similar conditions as aforementioned in Section 2.2. All components: CeO_2 precursor, 10Sc1CeZr, intermediate layer composition (10Sc1CeZr + CeO_2) and anode functional layer (ceria-Co-Cu) were pelletised and submitted to dilatometry analysis from room temperature to 1000˚C with a 10˚C.min^{-1} heating rate.

This baseline cell was prepared with an electrolyte support (Scandia-ceria stabilised zirconia electrolyte - HIONIC by FuelCell Materials) that was around 150 µm thick. A strontium-doped lanthanum manganite - LSM - ($La_{0.8}Sr_{0.2}MnO_{3-\delta}$ by Praxair) cathode was screen-printed onto a facet of the electrolyte and sintered at 1100˚C. The anode functional layer was then finally screen-printed onto the other side of the electrolyte support and sintered at 900˚C to avoid spinel phase decomposition (Co_3O_4 → CoO) at higher temperatures.

As for the optimised cell, the intermediate layer was first coated over the electrolyte and sintered at 1300˚C for 4 hours. The cathode and the anode were then analogously fabricated using identical

conditions to the baseline cell. The layer assembly configuration of the cells is depicted in Figure 1a, for the baseline cell and Figure 1b for the intermediate layered cell. In addition, with respect to enhancing the electrolyte/anode coherence, it is important to highlight that this transition intermediate anode layer should also maintain operational electronic/ionic conductivity so as not to hinder the activity within the anode functional layer. Moreover, the porous rough intermediate layer is expected to serve as better anchorage to the anode particles than the dense smooth electrolyte layer, thus allowing the anode to be sintered at such lower temperatures (900˚C).

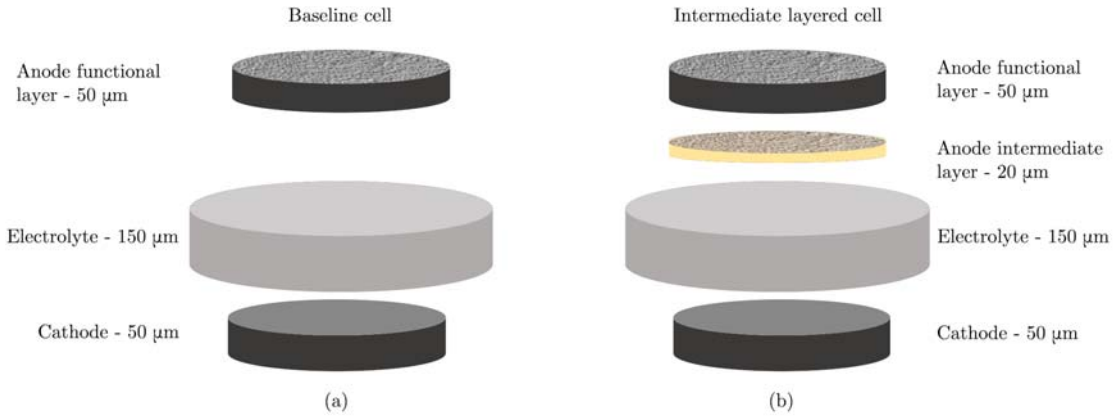

Figure 1. Assembly scheme of both (a) baseline and (b) intermediate layered cell.

Over both types of cells, silver wires from Scientific Wire Company and silver paste from Shanghai Research Institute of Synthetic Resin were used as lead wire and current collector. For the sake of simplicity, from here onwards the cells will be named “baseline cell” and “intermediate layered cell”.

2.4 Cell testing and characterisation

Cells were mounted onto an alumina tube and sealed at both sides with *Thermiculite*, from *Flexitallic*. The weight of the vertical tubing set-up was conveniently used to incur pressure over the sealing gaskets. The anode chamber was purged with 99.99% pure nitrogen (20 $mL.min^{-1}$) from room temperature to 650˚C until the reduction of the anodes started with hydrogen (30 $mL.min^{-1}$). The cells were tested first with hydrogen and then with dry methane as fuels at various temperatures. Instead of air, pure oxygen was used on the cathode side to avoid any source of cathodic polarisation, since the cathode was not the object of the present study. Electrochemical impedance spectroscopy (EIS) analysis was performed at open circuit voltage (OCV) with 10 mA of perturbation amplitude and at a frequency range from 1 MHz

to 50 mHz at 850˚C. After operation, the cell tests were terminated with flowing nitrogen (20 mL.min^{-1}) at the anode side to avoid carbon oxidation prior to the post-mortem analysis.

Samples of the electrocatalyst powder (heat-treated at 800˚C in air and named reference powder, reduced in hydrogen or reduced in methane) and post-mortem anode surfaces that had been operated with methane for over 24 hours were subjected to Raman spectroscopy to assess the eventual presence of carbon using a laser wavelength of 633 nm with 20% of the laser's total power density.

In addition to the Raman investigation, temperature-programmed oxidation - TPO - was performed over the operated intermediate layered cell to confirm that the material was coke-resistant. The test was done using a gas chromatograph, GC-2014 by Shimadzu, that was able to measure the outlet product amounts of an operated anode sample in an oxidising atmosphere (10% O_2 + balanced N_2) subjected to increasing temperature. The test rig was validated by first performing TPO in an aliquot of graphite with known mass. Similar to the Raman investigation, TPO was carried out over the anode sample operated for more than 24 hours with dry methane. It is important to highlight the cells were cooled under a 99.99% pure nitrogen atmosphere to prevent any eventually deposited carbon to be oxidised whilst shutting down.

The anode cross-sections were subjected to scanning electron microscopy (SEM) and energy dispersive X-ray spectroscopy (EDX). The EDX images of each element position were filtered with low-pass filters to eliminate most of the noise. Each filtered image map was then merged into a single image in which different colours were employed for phase segmentation.

3. Results and discussion

3.1 Powder characterisation

The XRD results for the anode electrocatalyst are shown in Figure 2a. The analyses were run over two different aliquots, first for the as synthesised powder right after the ashes were pulverised, represented as a dashed red line, and second for the electrocatalyst calcined in air at 800˚C. The narrowing of the peaks can be identified, indicating crystallisation in the as synthesised powder. Additionally, the formation of CeO_2, Co_3O_4, and CuO as isolated phases is also noted.

The formation of the spinel phase of cobalt oxide can be expected, taking into account the CeO_2-CoO phase diagram [25], which states that ceria will coexist as an isolated phase alongside with Co_3O_4 from room temperature to approximately 850˚C, if under an oxidising atmosphere [26]. However, at

temperatures higher than 850˚C, Co_3O_4 would be decomposed to CoO. The CeO_2-CoO system is predicted to form no solid solution in an oxidising atmosphere. Additionally, the phase diagram also indicates that, for a cobalt-rich system, with more than 50 mol% of Co, the system is expected to be in a metastable state at temperatures above 1000˚C, where the sample can melt, especially if the particles size distribution is nanometric. In reducing atmospheres, although there are several solid solutions that can be formed between Ce and Co [27], this is less likely to occur since ceria is rarely fully reduced. Concerning the Ce-Cu system, the same applies, since ceria is very stable and is less likely to become fully oxygen-deficient, and also due the atomic radii mismatches between Ce and Cu [28]. Additionally, solid solutions between CeO_2 and Cu would also not be expected [29]. The cobalt and copper binary systems show low solubility into each other, indicating that, under reducing conditions, these metals will also coexist as isolated phases. This leads to the conclusion that the actual anode material will be a three-phase compound such as $CeO_{2-\delta}$-Co-Cu. Rietveld refinement over the XRD data for this catalyst composition was performed in our previous work [18] and is herein presented in Table 1 as a means to corroborate the statement of isolated phase formation that was seen within the XRD patterns. The low deviation between the calculated Rietveld lattice parameters and the values presented in corresponding PDF files in Table 1 confirms the conclusion of isolated oxide formation. The details of the Rietveld applied methodology are described elsewhere [18].

Although not show in the phase diagram, the slight distortion of the calculated lattices may indicate the formation of small amounts of solid solutions, mainly between CeO_2-Cu. In stoichiometric ceria (CeO_2), the ionic radii of cerium Ce^{4+}/Ce^{3+} are 102/118 pm and thus very close to that of Cu^+, which is 96 pm. Therefore, if the as-synthesised powder presents Cu^+ (Cu_2O), the presence of small amounts of $Ce_{1-x}Cu_xO_{2-\delta}$ is possible [30]. However, this does not apply when CuO (Cu^{2+}) presence is the case.

Table 1. Lattice parameters calculated by Rietveld refinement [18].

Oxide	Space Group	Source	a [nm]	b [nm]	c [nm]	α [˚]	β [˚]	γ [˚]	Coeff.
CeO_2	Fm-3m	Calculated	0.5409(5)	0.5409(5)	0.5409(5)	90.00	90.00	90.00	R_p=27.8
		PDF-03-065-2975	0.5409	0.5409	0.5409	90.00	90.00	90.00	
Co_3O_4	Fd-3m	Calculated	0.804(6)	0.8074(6)	0.8074(6)	90.00	90.00	90.00	R_{wp}=15.6
		PDF-00-042-1467	0.8074	0.8074	0.8074	90.00	90.00	90.00	
CuO	C 2/c	Calculated	0.4696(4)	0.3408(0)	0.5127(5)	90.00	99.66	90.00	χ^2=1.14
		PDF-04-007-1375	0.4684	0.3423	0.5129	90.00	99.54	90.00	

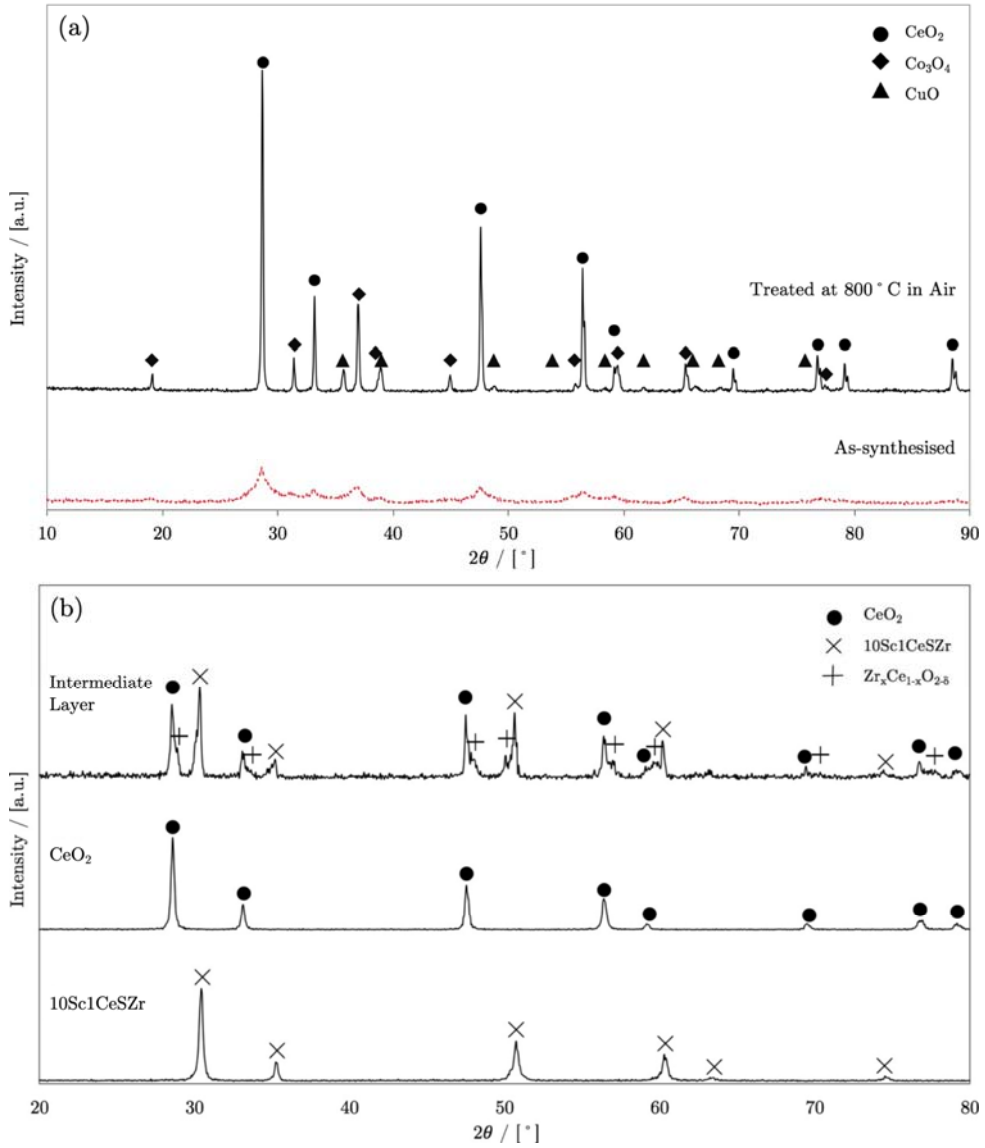

Figure 2. XRD pattern: (a) for the catalyst powder as synthesised and treated at 800˚C in air and (b) the sintered intermediate layer and its isolated precursors.

The results for composition estimation by the Rietveld method are presented in Table 2 and are compared to the composition measured by XRF over the same powder. The composition results are fairly consistent with the results expected upon designing the synthesis strategy.

Table 2. Molar amount of compounds calculated by Rietveld refinement, measured with XRF and expected upon synthesis.

Element	Molar Composition [%]		
	Rietveld	XRF	Expected
Ce	50.93	52.86 ± 0.64	50.00
Co	24.50	23.43 ± 0.61	25.00
Cu	24.57	23.71 ± 0.5	25.00

In Figure 2b, the diffraction patterns for the sintered intermediate layer as well as its precursors are shown for comparison. The most notable result is the partial phase transformation from CeO_2 and 10Sc1CeSZr to the well-known Zr-Ce non-stoichiometric solid solution [31]. It is important to highlight that this phase was formed at high temperatures, such as 1300˚C, where diffusion is favoured.

Cerium has a broad solubility into the zirconia lattice when starting from sintering temperatures towards cooling and particularly within the intermediate layer composition (42 mol% of ceria), as per the ZrO_2-CeO_2 phase diagram [31]. Furthermore, upon cooling from 800˚C, most of the $(CeO_2)_{0.4}$-$(ZrO_2)_{0.6}$ phase will be decomposed peritectoidally into ceria cubic fluorite phase - $CeO_{2(css)}$ - and tetragonal zirconia - $ZrO_{2(tss)}$, according to Equation 3. However, since in this case the zirconia structure is stabilised with scandia, the fluorite-type of the stabilised zirconia is also expected. On the other hand, composition of the intermediate layer is placed outside the phase's miscibility gap (20–24 mol% of CeO_2), where the phases are most likely to coexist isolated, thus keeping ceria's electronic conductivity.

The 10Sc1CeSZr electrolyte is reported to have interesting features such as high stability at high temperatures over long-term operation [32]. Lee *et al.* [33] found that after 100 hours at 800˚C, 10Sc1CeSZr did not undergo any phase transformation from a cubic to rhombohedral structure.

$$Zr_{0.6}Ce_{0.4}O_2 \xrightarrow[peritectoid]{} ZrO_{2_{(tss)}} + CeO_{2_{(css)}} \qquad (at\ 800^{\circ}C) \tag{3}$$

The TPR profiles for both cycles are shown in Figure 3a. The first consumption peak notably decreased within the second cycle. On the other hand, the second peak showed increased area, compensating the former. The three peaks from 190 to 303˚C in the TPR profiles of both cycles are assigned to cobalt and copper oxides, which tend to be fully reduced to Co and Cu in this temperature range [34-38].

Cerium oxide will be partially reduced, which will result in an oxygen-deficient structure that is suitable to operate as a mixed ionic and electronic conductor, as shown in Equation 4. Furthermore, ceria tends to be partially reduced in two different stages, which requires distinct amounts of energy for each to occur. First, oxygen placed over the surface of the octahedral structure of ceria is removed and then its bulk will also be partially reduced [34, 35, 39]. Therefore, the last two peaks at higher temperatures are assigned to ceria's surface reduction for the former and to its bulk for the latter.

$$CeO_2 + \delta H_2 \rightarrow CeO_{2-\delta} + \delta H_2O \quad (4)$$

Consequently, ceria's capability to receive oxygen ions is enhanced under reducing conditions, according to Equation 5.

$$Ce_{Ce}^{\times} + O_O^{\times} + \delta H_2 \rightarrow 2\delta Ce_{Ce}' + (1-2\delta)Ce_{Ce}^{\times} + \delta V_{\ddot{O}} + (1-\delta)O_O^{\times} + H_2O \quad (5)$$

The Kroger-Vink notation in Equation 5 shows that the original ceria structure undergoes partial reduction, leaving Ce^{4+} and Ce^{3+} cations, $Ce_{Ce}^{\times}$ and Ce_{Ce}', respectively, and thus consequently becoming oxygen-deficient and releasing oxygen anions, $V_{\ddot{O}}$ and $O_O^{\times}$, respectively.

Table 3 shows the percentage areas represented by each peak at the first and second cycles. Again, the decrease of peaks 1 and 3 with respect to peak 2 from the first to second cycles is notable, whereas ceria reduction (peaks 4 and 5) remained almost constant. The total amount of hydrogen consumed was 5.70×10^{-3} and 5.82×10^{-3} mol per catalyst gram in the first and second cycles, respectively.

Table 3. Estimated hydrogen consumption at each H_2-TPR cycle.

TPR Peaks	First Cycle		Second Cycle	
	Area [%]	H_2 Consumption [$\times 10^{-3}$ mol.g^{-1}]	Area [%]	H_2 Consumption [$\times 10^{-3}$ mol.g^{-1}]
Peak 1	21.05	1.20	15.55	0.91
Peak 2	26.05	1.48	35.55	2.07
Peak 3	23.25	1.33	18.49	1.08
Peak 4	14.18	0.81	14.70	0.86
Peak 5	15.47	0.88	15.70	0.91

In Figure 3b, the 100 µL pulses of oxygen uptake are presented. It took eleven full injections of 100 µL for the TCD to start measuring any amount of oxygen consequently passing through the sample without being reduced. Thereafter, four injections were partially consumed until full oxidation could be observed after 15 injections, accounting for 2.90×10^{-3} mol of oxygen per catalyst gram for both cycles. It is notable that the ratio between hydrogen consumed and oxygen uptake is close to two, which is consistent to what would be theoretically expected. Additionally, accounting for the last two peaks of each TPR profile and comparing to stoichiometric cerium oxide, the oxygen deficiency can be estimated

as approximately 11% in both cases, which corresponds to $CeO_{1.78}$ as the final composition after reduction.

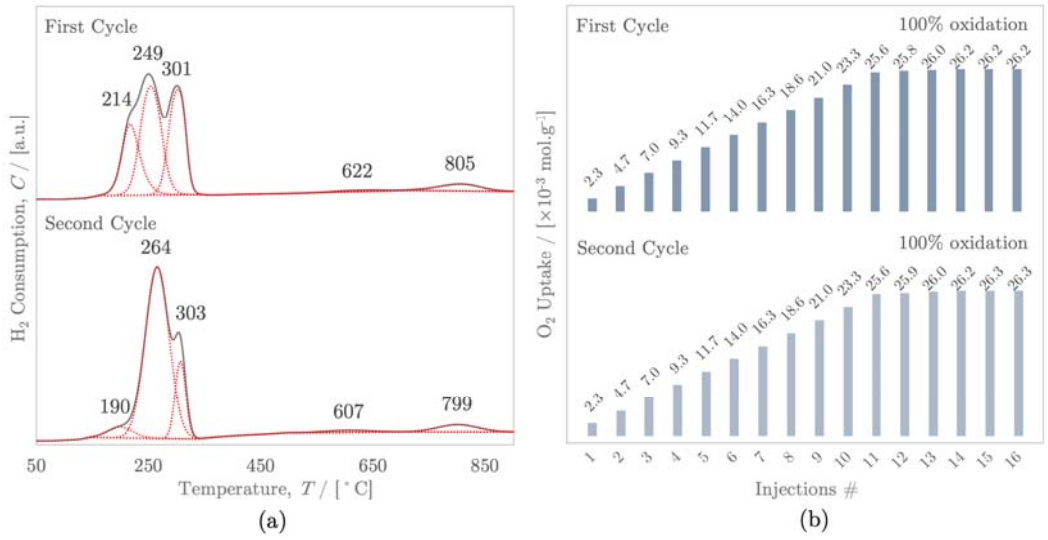

Figure 3. (a) H2-Temperature-programmed reduction profile of each cycle (Adapted from our previous work [18] with Elsevier's permission) (b) pulse-controlled oxidation showing oxygen uptake in both cycles.

From the TPR/PCO cycling test it is markedly observed that the maximum hydrogen consumption has been displaced from 249 to 264˚C. Therefore, regarding the stability of the catalyst, some conclusions can be drawn regarding redox cycling such as the evolution of the microstructure due to particle size changes between phases or even agglomeration of the metallic compounds upon reducing. However, since the overall hydrogen consumption and oxygen uptake remained almost identical, it can be concluded that the activity of the catalyst remained steady after these two cycles.

In Figure 4a the dilatometry analysis data are plotted against temperature. To estimate the coefficient of thermal expansion of each compound a third order regression was applied to each data set aiming at obtaining a coefficient of correlation (R^2) higher than 0.9999. The regression thus assumes that the experimental data set follows Equation 6.

$$\frac{\Delta L}{L_0} = c_1 + c_2 T + c_3 T^2 + c_4 T^3 \quad (6)$$

where ΔL is the difference between a current length (at a given temperature) and the sample initial length (L_0), T is the temperature, and c_i are the experimental constants. Consequently, to obtain the CTE

as a function of temperature, Equation 6 is thus differentiated in respect to the temperature, as shown in Equation 7 as follows.

$$\alpha = \frac{1}{L_0}\left(\frac{dL}{dT}\right) = c_2 + 2c_3T + 3c_4T^2 \quad (7)$$

where α is the CTE as a function of temperature. The experimental constants are presented in Table 4 at each temperature range considered for each sample. The CTE behaviour against temperature could then be calculated using Equation 7 and is represented in Figure 4b. In Figure 4a the smooth transition from anode functional layer to electrolyte, when the intermediate layer is concerned is markedly. From Figure 4b it can be estimated that in a range of temperatures such as 600-800˚C the CTE varies from 11.1 to 11.3 $^{\circ}C^{-1}$ for the 10Sc1CeSZr, from 18.0 to 18.3 $^{\circ}C^{-1}$ for the CeO_2 precursor and from 14.3 to 14.6 $^{\circ}C^{-1}$ for the intermediate layer (10Sc1CeSZr + CeO_2). As for the anode functional layer (ceria-Co-Cu), these values lie from 14.6 to 15.0 $^{\circ}C^{-1}$, thus confirming more adequacy with the intermediate layer than with the electrolyte (10Sc1CeSZr). Moreover, it can be noted that from 830˚C onwards, the ceria-Co-Cu sample starts to shrinkage, indicating sintering behaviour, thus confirming that such temperatures are enough high to consolidate this anode layer. Therefore, the CTE for this material was estimated within the 25-830˚C temperature range.

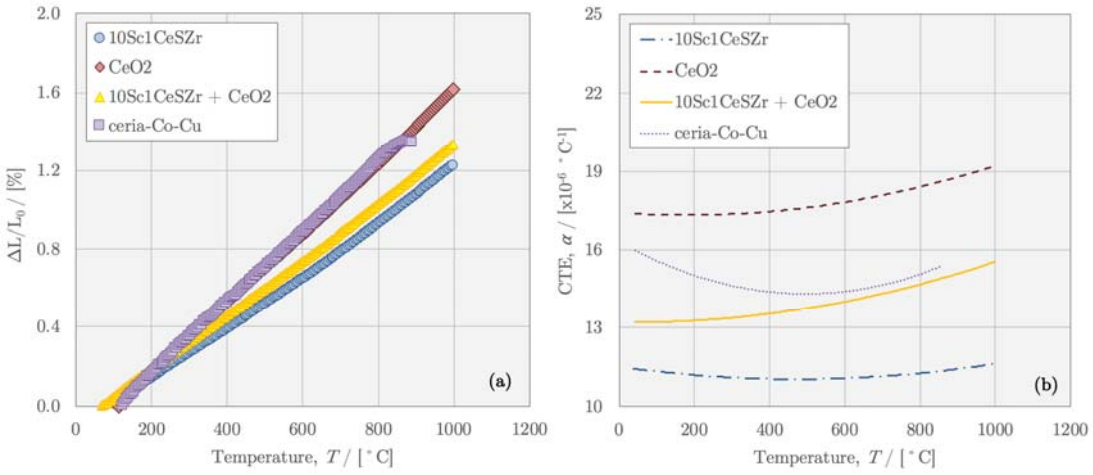

Figure 4. (a) Dilatometric analysis of CeO_2, 10Sc1CeSZr, CeO_2 + 10Sc1CeSZr (intermediate layer) and ceria-Co-Cu anode functional layer and (b) CET behaviour against temperature.

It is important to highlight that the anode functional layer dilatometric behaviour was assessed when the material was still in its oxidising state and thereby, under operation at reducing atmosphere the Co and

Cu metallic phases will increase the CET of the material, which reinforces the necessity of the intermediate layer.

Table 4. Experimental constants from Equation 6 and the correlation factors for each 3rd order regression.

Material	Temperature Range [˚C]	Regression coefficients				
		c_1	c_2	c_3	c_4	R^2
10Sc1CeSZ	25 - 1000	$-9.59x10^{-4}$	$1.15x10^{-5}$	$-1.00x10^{-9}$	$7.07x10^{-13}$	> 0.9999
CeO_2	25 - 1000	$-1.70x10^{-3}$	$1.74x10^{-5}$	$-5.07x10^{-10}$	$9.40x10^{-13}$	> 0.9999
10Sc1CeSZ + CeO_2	25 - 1000	-7.69x10-^{4}	$1.32x10^{-5}$	$-9.11x10^{-11}$	$8.41x10^{-13}$	> 0.9999
ceria-Co-Cu	25 - 830	$-1.78x10^{-3}$	$1.63x10^{-5}$	$-4.03x10^{-9}$	$2.71x10^{-12}$	> 0.9999

3.2 Electrochemical Performance

Figure 5 unveils an ensemble of electrochemical performance results for both types of cells tested using either hydrogen or methane as fuels. Figure 5a presents i-V plots of the tests performed with dry hydrogen as fuel, for both the baseline cell (BLC) and intermediate layer cell (ILC). The BLC was tested at 750, 800, and 850˚C, showing maximum power densities of 59, 102, and 152 $mW.cm^{-2}$ and OCVs of 1.00, 1.00, and 0.99 V, respectively. At these same conditions, ILC cells were able to deliver 176, 273 and 363 $mW.cm^{-2}$ with OCV values of 1.02, 1.02, and 1.00 V, respectively.

Figure 5b depicts the electrochemical results when the fuel stream was switched to dry methane. The cells (BLC and ILC) were then subjected to electrical load at 800 and 850˚C. Although the baseline cells presented low power densities under these conditions – 11 and 37 $mW.cm^{-2}$ – OCVs values of 1.03 and 1.22 V suggest that adequate sealing was achieved. On the other hand, the IL cell shows significantly higher results in these same conditions, for which the maximum power densities were 150 and 200 $mW.cm^{-2}$, whereas the OCVs were 1.00 and 1.03 V, respectively, at 800 and 850˚C.

It can be observed that adequate OCVs during all the aforementioned tests were obtained, suggesting that no leakages or gas mixing occurred throughout the electrolyte, as expected for a 150 μm-thick electrolyte support, and also that the cell was properly sealed. The SOFC power density increased 2.4x with hydrogen and 5.5x with dry methane as fuels after the CeO_2-ScCeSZ intermediate layer was inserted. The increase in OCV with increasing temperature for the methane-fed cells is consistent with the literature, both theoretically [40] and experimentally [41, 42].

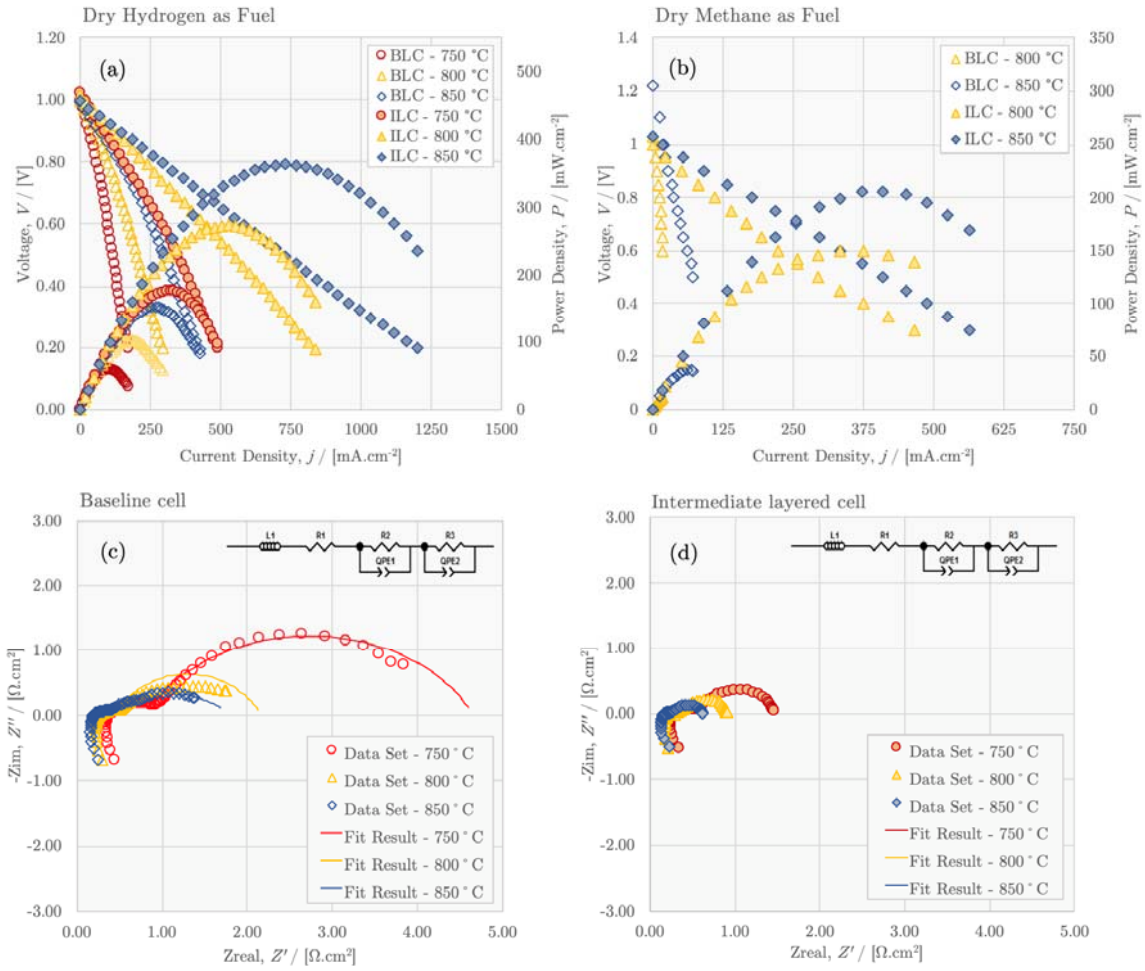

Figure 5. i-V plots for both baseline cell (BLC) and intermediate layered (ILC) cell (a) with hydrogen and (b) dry methane as fuel. EIS spectra with hydrogen as fuel for the (c) baseline cell and (d) intermediate layered cell.

In Figures 4c and 4d, the Nyquist plots for the baseline cell and intermediate layered cell are respectively presented. The impedance plots were recorded whilst dry hydrogen served as fuel at temperatures of 750, 800, and 850˚C. Qualitatively, the differences in the arc size amongst cells are notable, showing that both ohmic and total polarisation are higher in the case of the baseline cell. The ohmic resistances are estimated from the plot as being 0.41, 0.26, and 0.20 $\Omega.cm^2$ for the baseline cells and 0.27, 0.20, and 0.15 $\Omega.cm^2$ for the intermediate layered cells at 750, 800, and 850˚C, respectively. The total polarisation for both cells at all temperatures was estimated both from the Nyquist plot and by ohmic law applied to the i-V plots of Figure 5a. Regarding the Nyquist plot, an element circuit model consisted of a resistance in series with two parallel RQs (resistance and constant phase element), R2Q1 and R3Q2, was used to fit the data and estimate total polarisation. The dataset is represented in all spectra as open symbols whereas the fitting model is denoted by a continuous line. The results are presented in

Table 5. The polarisation estimated from both methods shows consistency amongst them and the differences in resistance by a factor of 2-3x are notable.

Table 5. Total polarisation estimated from the Nyquist plot and the i-V (Ohm's law) for both cells.

Temperature	Baseline Cell		Intermediate Layered Cell	
[˚C]	Nyquist [Ω.cm2]	i-V plot [Ω.cm2]	Nyquist [Ω.cm2]	i-V plot [Ω.cm2]
750˚C	4.59	4.68	1.48	1.69
800˚C	2.13	2.73	0.91	0.99
850˚C	1.68	1.89	0.62	0.67

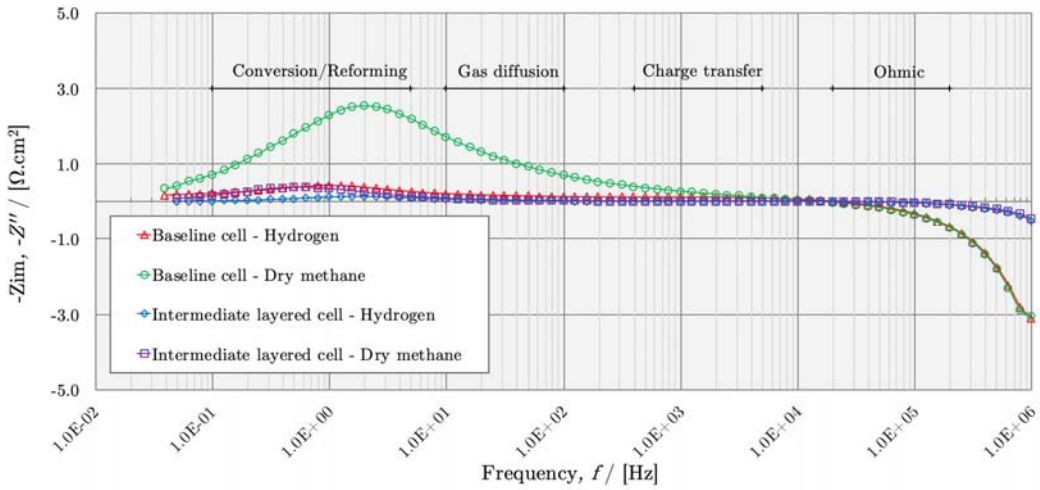

Figure 6. Bode plot for both cells in hydrogen and dry methane at 850˚C.

Since all other elements used, such as current collectors, cathode, and electrolyte, were identical for the configuration of both cells, the almost doubled ohmic resistance can be attributed to the poor interface between the anode and electrolyte for the baseline cell. It is known that ohmic resistance is mainly associated with ionic transport and sensed at high frequencies such as 20 kHz or higher. Responses in the range of frequencies of 5 to 0.5 kHz are associated with charge transfer on three-phase boundaries - TPB - and exchange currents. The effects of gas diffusion can be observed in the range of 100 to 10 Hz, whereas gas conversion or reforming processes as sources of impedance, can be identified at lower frequencies such as 5 to 0.1 Hz [43-45]. Moreover, it can be said that processes occurring at low frequencies such as gas diffusion through the microstructure and channels as well as fuel conversion/reforming can be linked to mass transfer. At higher frequencies, phenomena such as

dissociative adsorption of fuel molecules, oxidation, and electrochemical reactions on TPB sites, are charge transfer processes [43, 44].

Therefore, the Bode plot of impedance spectroscopy results for both baseline and intermediate layered configurations, shown in Figure 6, highlights the gains experienced with the addition of the intermediate layer between the anode/electrolyte interface. The first notable result is the evident high values at high frequencies for both fuel situations. This indicates poor ionic/electronic transfer, which can be associated with the anode/electrolyte thermal mismatches when operating in a reducing atmosphere at high temperatures such as 850˚C. The second interesting result is the huge difference in impedance from 0.1 to 100 Hz for the baseline cell operating with methane. The fuel conversion ability also increased with the insertion of the intermediate layer, due to ceria's already proven high activity for methane conversion and carbon oxidation [18, 46-48].

3.3 Post-mortem characterisation

The Raman spectroscopy analysis was conducted to assess the eventual presence of carbon deposition on the anodes tested under methane fuel for over 24 hours and it was compared with the spectra measured on the samples that were oxidised and reduced in hydrogen and in methane, respectively. As can be seen in Figure 7, for the oxidised anode, the peaks located at 196, 482, 523, 621, and 691 cm^{-1} are related to Co_3O_4 [49, 50] and the peak at 462 cm^{-1} is assigned to CeO_2 [51]. The Raman shift at 286 and 347 cm^{-1} corresponds to CuO and that at 158, 219 cm^{-1} to Cu_2O [52]. Finally, peaks at approximately 1338, 1580, and 2660 cm^{-1} are assigned to carbon for the G, D, and 2D bands [53].

The ceria peak at 462 cm^{-1} can be assigned to the Ce F_{2g} mode due to symmetrical stretching of the Ce-O vibrational unit in the octahedral coordination [54, 55]. The absence of a fluorite-type structure at 600 cm^{-1} suggests that solid solutions were most likely not formed [56], which is consistent with the previous X-ray discussion. In addition, broadening and shifting of the Ce F_{2g} band indicate that ceria's particle size would have changed in the case of nanoparticles [56], which is not the case here. However, since this peak at 462 cm^{-1} remains sharp in all cases, the slight shifting can be assigned to an oxygen-deficient ceria lattice [57]. The Raman peaks of crystalline Co_3O_4 are related to E_g (482 cm^{-1}), F_{2g} (523 and 621 cm^{-1}), and A_{1g} (691 cm^{-1}) modes [37, 58, 59]. CuO modes A_{1g} and B_g are at 286 and 347 cm^{-1}. Additionally, Cu_2O peaks were found at 158, 219, and 550 cm^{-1}.

The Raman spectroscopy results confirm that traces of carbon were found in the spectrum referred to the aliquot of powder that was exposed to methane whereas no carbon traces were found over the anode surface after operating with pure methane for over 24 hours. Therefore, the Raman results indicate that the catalyst itself combined with thermal energy converts methane into hydrogen and carbon by cracking, whilst as an electrocatalyst methane is electrochemically oxidised under current flow rather than being cracked. These results suggest that if the cell runs at OCV or even at low current conditions for a long time it might be prone to carbon deposition, whereas under fuel utilisation electrochemical oxidation takes place and carbon is thus fully oxidised by the oxygen ions.

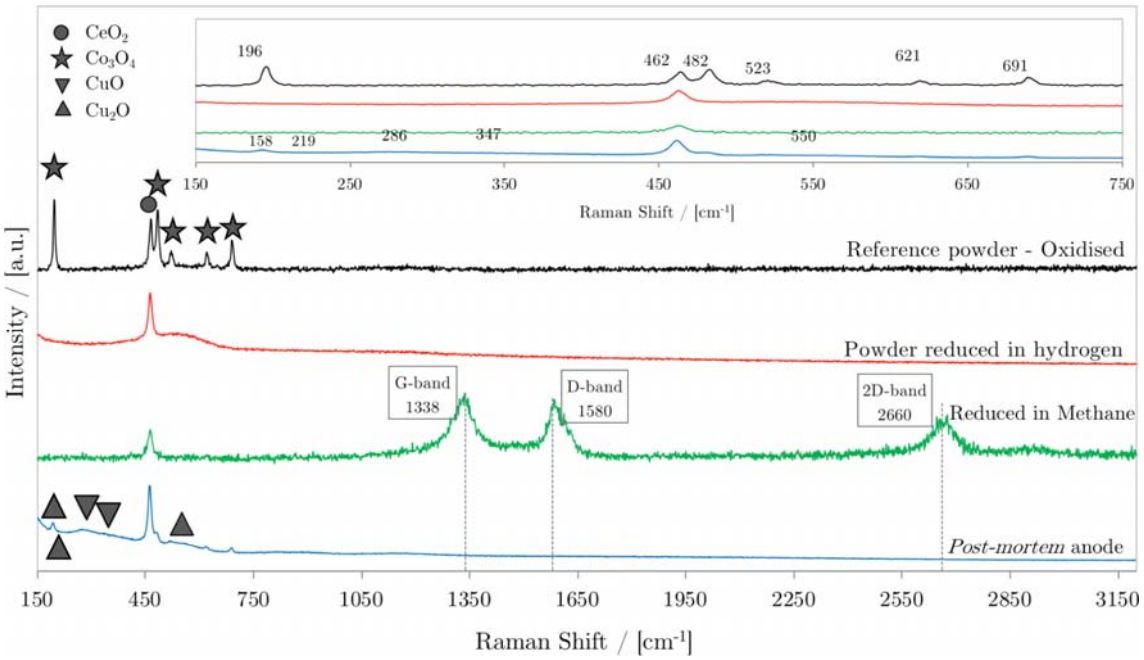

Figure 7: Raman spectroscopy over different aliquots of powder that were heat treated in air, reduced in hydrogen and reduced in methane as well as a post-mortem anode operated with dry methane for 24 hours.

Furthermore, TPO results are presented in Figure 8. This figure shows the carbon oxidation profile for 1.26 mg of graphite powder as a baseline and the equivalent carbon that was deposited over the intermediate layered anode after operation. It is important to highlight the consistency of the graphite peaks, which validates the TPO experimental setup of this work. From 250 to 350˚C a small area is observed, as expected for amorphous carbon, and the highest carbon oxidation processes occur from 550 and 800˚C and can be assigned to graphitic carbon [60].

Moreover, from the oxidation profile of the anode it was estimated, by relative area, that 0.29 mg of carbon remained over the bulk anode. Taking into account the anode volume, the normalised mass of

carbon is 0.19 g of carbon per cm^3 of anode material, which may be considered negligible for impacting the adequate anode operation considering that it represents less than 5% of the anode's total mass. Additionally, taking into account that no visual carbon was found after dismantling the cells, the coke resistance in this case is thereby well-proved.

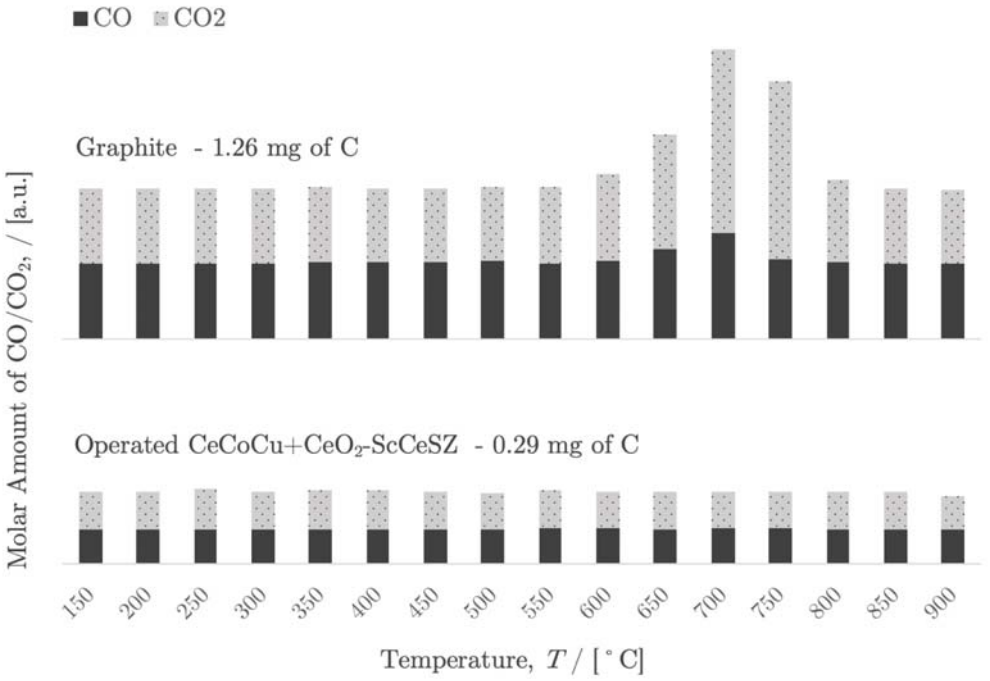

Figure 8: Temperature-programmed oxidation profile for graphite powder and the operated intermediate layered cell.

The lower power density results with dry methane when compared to those in hydrogen could be elucidated by the fact that the system was dominated by the concentration polarisation whilst running with heavier fuels such as methane [4]. It also should be pointed out that an electrolyte-supported cell was used in the present work, which might result in lower performance, due to higher ohmic polarisation. The high-resolution SEM cross-section images, presented in Figures 9a and 9b, show the baseline cell and the intermediate-layered cell, respectively. In Figure 9a, the anode layer is approximately 53 μm, whereas in Figure 9b, the well-defined CeO_2-ScCeSZ scaffold is 23 μm, followed by the anode active layer with around 60 μm thickness. Both Figures 9a and 9b show inserts with details of each interface and an EDS mapping distribution of phases. The segmented images inserted in Figure 9a and 9b show Zr, Ce, Co and Cu in purple, yellow, red and blue, respectively. Observing the mapping inserts, the differences between the layers are notable, and the presence of the intermediate layer shows that the microstructure changes

gradually towards the anode surface. Furthermore, the detailed image of the anode/electrolyte interfaces show drastic differences between Figure 9a and 9b, with significant higher coherence between the intermediate layer and the electrolyte (9b) when compared to the baseline cell (9a). Moreover, in all inserted images particles look well-sintered, thus confirming that the abovementioned sintering temperatures of 1300˚C and 900˚C were adequate for the intermediate and anode functional layers, respectively, which for the anode layer is corroborated by the dilatometry results.

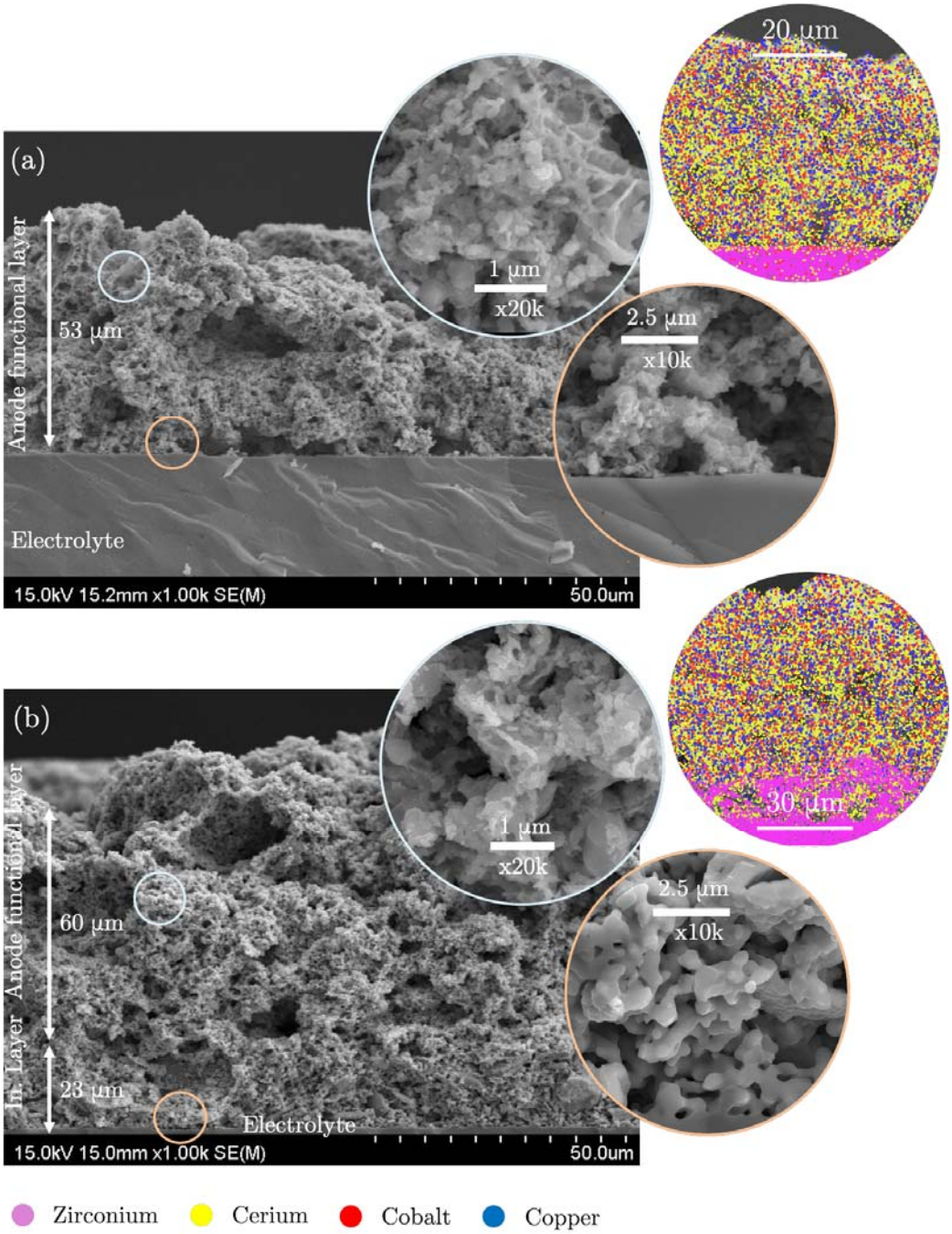

Figure 9: Cross section SEM images for (a) baseline cell and (b) intermediate layered cell with details of the interface and their EDX mapping showing phase distribution.

The enhanced oxygen storage capacity (OSC) of CeO_2 is reported in the literature. Renuka *et al.* [61] have shown that the presence of ceria nanoparticles may have a supercharging effect in the OSC of such materials. This indicates that ceria-based compounds are a qualified choice to serve as an intermediate layer in the case of an SOFC anode. In the present work, mixing ceria with an electrolyte material has increased the thermal compatibility between the anode and electrolyte. The presence of porous electrolyte material near the dense electrolyte enhances the triple phase boundaries within this highly active spot. The fact that the intermediate layer is composed both by scandia-stabilised zirconia and ceria also makes it more chemically compatible with both structures, the electrolyte itself and the anode functional layer, bridging these components all together.

Moreover, by successfully inserting this intermediate layer, the manufacturing process could be simplified due to the utilisation of an industrial-like manufacturing process such as screen printing rather than laborious impregnation steps.

4. Conclusions

Nickel-based anodes are the current state-of-the-art for SOFC technology when hydrogen is used as fuel. However, the need for nickel-free material development has been recognised due to the deleterious effects of carbon deposition when alcohols and hydrocarbons are fed directly to the anode.

This work highlights the importance of inserting an anode intermediate layer within a nickel-free SOFC anode configuration. By increasing the anode/electrolyte coherence, the cell was able to operate with two to five times higher power densities. In addition, as observed in Raman spectroscopy, the operated fuel cell has not shown evidence of carbon over its surface, whereas the standalone catalyst was prone to carbon deposition. This indicates that, under electrochemical conditions, any carbon remaining in the anode microstructure will most likely be electro-oxidised under oxygen ions presence. Furthermore, a TPO analysis corroborated the Raman results, by quantitatively showing negligible traces of carbon within the cell that was operated for over 24 hours.

The insertion of the CeO_2-ScCeSZ intermediate layer is essential to enhance the adhesion between the electrolyte and anode by anchoring the anode functional layer particles. Moreover, the intermediate layer was expected to enhance oxygen ion transfer near the electrolyte/anode interface and increase the

electrocatalytic activity to methane conversion due the addition of ceria, which is a mixed ionic electronic conductor.

Acknowledgements

This work was supported by the Brazilian National Council of Technological and Scientific Development (CNPq) regarding a Split Fellowship PhD program, registered under the award number 200665/2015-4 and thus gratefully acknowledged by one of us (B.J.M.S.). The financial support to this work by BNDES and by the enterprises Oxiteno S.A. and EnergiaH Ltda. is also acknowledged. This study was financed in part by the Coordenação de Aperfeiçoamento de Pessoal de Nível Superior – Brasil (CAPES) – Finance Code 001. The authour, J.E.H., also acknowledges the financial support from the Technology Development Program to Solve Climate Changes of the National Research Foundation (NRF) funded by the government (Ministry of Science and ICT) of the Republic of Korea (NRF-2017M1A2A2044926).

References

[1] A. J. M. Araujo, A. R. O. Sousa, J. P. F. Grilo, L. F. A. Campos, F. J. A. Loureiro, D. P. Fagg, R. P. S. Dutra, D. A. Macedo, Preparation of one-step NiO/Ni-CGO composites using factorial design, Ceram. Int. 42 (2016) 18166-18172. https://doi.org/10.1016/j.ceramint.2016.08.131.

[2] J. Xiao, X. Zeng, M .Li, P. Dong, H. Wu, M. Xu, Y. Lin, J. Liu, Y. Xie, Y. Zhang, Effect of pre-calcined ceramic powders at different temperatures on Ni-YSZ anode-supported SOFC cell/stack by low pressure injection molding, Ceram. Int. Available online 29 June 2019 https://doi.org/10.1016/j.ceramint.2019.06.270.

[3] M. J. Escudero, I. G. de Parada, A. Fuerte, J. L. Serrano, Analysis of the electrochemical performance of MoNi-CeO_2 cermet as anode material for solid oxide fuel cell. Part I. H_2, CH_4 and H_2/CH_4 mixtures as fuels., J. Power Sources 253 (2014) 64–73. https://doi.org/10.1016/j.jpowsour.2013.12.027.

[4] H. Aslannejad, L. Barelli, A. Babaie, S. Bozorgmehri, Effect of air addition to methane on performance stability and coking over NiO-YSZ anodes of SOFC., Appl. Energ. 177 (2016) 179–186. https://doi.org/10.1016/j.apenergy.2016.05.127.

[5] D. Saebea, S. Authayanun, Y. Patcharavorachot, W. Paengjuntuek, A. Arpornwichano, Use of different renewable fuels in a steam reformer integrated into a solid oxide fuel cell: Theoretical analysis and performance comparison., Energy 51 (2013) 305–313. https://doi.org/10.1016/j.energy.2012.12.014.

[6] A. Lanzini, P. Leone, C. Guerra, F. Smeacetto, N. P. Brandon, M. Santarelli, Durability of anode supported Solid Oxides Fuel Cells (SOFC) under direct dry-reforming of methane., Chem. Eng. J. 220 (2013) 254–263. https://doi.org/10.1016/j.cej.2013.01.003.

[7] M. Liu, A. van der Kleij, A. H. M. Verkooijen, P. V. Aravind, An experimental study of the interaction between tar and SOFCs with Ni/GDC anodes., Appl. Energ. 108 (2013) 149–157. https://doi.org/10.1016/j.apenergy.2013.03.020.

[8] S. Li, W. Pan, S. Wang, X. Meng, C. Jiang, J. T. S. Irvine, Electrochemical performance of different carbon fuels on a hybrid direct carbon fuel cell., Int. J. Hydrogen Energ. 42 (2017) 16279–16287. https://doi.org/10.1016/j.ijhydene.2017.05.150.

[9] B. He, Z. Wang, L. Zhao, X. Pan, X. Wu, C. Xi, Ti-doped molybdenum- based perovskites as anodes for solid oxide fuel cells., J. Power Sources 241 (2013) 627–633. https://doi.org/10.1016/j.jpowsour.2013.04.148.

[10] C. A. Silva, P. E. V. Miranda, Synthesis of $LaAlO_3$ based materials for potential use as methane-fueled solid oxide fuel cell anodes., Int. J. Hydrogen Energ. 40 (2015) 10002–10015. https://doi.org/10.1016/j.ijhydene.2015.06.019.

[11] S. A. Venâncio, P. E. V. Miranda, Direct utilization of carbonaceous fuels in multifunctional SOFC anodes for the electrosynthesis of chemicals or the generation of electricity., Int. J. Hydrogen Energ. 42 (2017) 13927–13938. https://doi.org/10.1016/j.ijhydene.2017.02.051.

[12] S.-I. Lee, K. Ahn, J. M. Vohs, R. J. Gorte, Cu-Co Bimetallic Anodes for Direct Utilization of Methane in SOFCs., Electrochem. Solid ST. Letter 8 (2005) A48–A51. https://doi.org/10.1149/1.1833678.

[13] S.-I. Lee, J. M. Vohs, R. J. Gorte, A Study of SOFC Anodes Based on Cu-Ni and Cu-Co Bimetallics in CeO_2YSZ., J. Electrochem. Soc. 151 (2004) A1319–A1323. https://doi.org/10.1149/1.1774184.

[14] A. Fuerte, R. X. Valenzuela, M. J. Escudero, L. Daza, Study of a SOFC with a bimetallic Cu-Co-ceria anode directly fuelled with simulated bio- gas mixtures., Int. J. Hydrogen Energ. 39 (2014) 4060–4066. https://doi.org/10.1016/j.ijhydene.2013.06.142.

[15] S. A. Venâncio, P. E. V. Miranda, Synthesis of $CeAlO_3/CeO_2$-Al_2O_3 for use as a solid oxide fuel cell functional anode material., Ceram. Int. 37 (2011) 3139–3152.https://doi.org/10.1016/j.ceramint.2011.05.054.

[16] S. A. Venâncio, P. E. V. Miranda, Solid oxide fuel cell anode for the direct utilization of ethanol as fuel., Scripta Mater. 65 (2011) 1065– 1068. https://doi.org/10.1016/j.scriptamat.2011.09.017.

[17] Y. Hiei, T. Ishihara, Y. Takita, Partial oxidation of methane for internally reformed solid fuel cell., Solid State Ionics 86-88 (1996) 1267–1272. https://doi.org/10.1016/0167-2738(96)00299-8.

[18] B. J. M. Sarruf, J.-E. Hong, R. Steinberger-Wilckens, P. E. V. de Miranda, CeO_2-Co_3O_4-CuO anode for direct utilisation of methane or ethanol in solid oxide fuel cells., Int. J. Hydrogen Energ. 43 (2018) 6340–6351. https://doi.org/10.1016/j.ijhydene.2018.01.192.

[19] B. J. M. Sarruf, J.-E. Hong, R. Steinberger-Wilckens, P. E. V. de Miranda, Ceria-Co-Cu-based SOFC anode for direct utilisation of methane or ethanol as fuels., Int. J. Hydrogen Energ., *In Press* Available online 2 May 2019. https://doi.org/10.1016/j.ijhydene.2019.04.075.

[20] W. L. Roth, The magnetic structure of CO_3O_4., J. Phys. Chem. Solids 25 (1964) 1–10.[21] I. B. Krynetskii, B. A. Gizhevskii, S. V. Naumov, E. A. Kozlov, Size Effect of the Thermal Expansion of Nanostructural Copper Oxide., Fizika Tverdogo Tela 50 (2008) 723–725. https://doi.org/10.1134/S1063783408040264.

[22] W. Fan, Z. Z.Wang, Y.Bai, J.W.Che, R.J.Wang, F.Ma, W.Z.Tao, G.Y.Liang, Improved properties of scandia and yttria co-doped zirconia as a potential thermal barrier material for high temperature applications., J. Eur. Ceram. Soc. 38 (2018) 4502- 4511.
https://doi.org/10.1016/j.jeurceramsoc.2018.06.002.

[23] H. Hayashi, M. Kanoh, C. J. Quan, H. Inaba, S. Wang, M. Dokiya, H. Tagawa, Thermal expansion of Gd-doped ceria and reduced ceria., Solid State Ionics 132 (2000) 227–233. https://doi.org/10.1016/S0167-2738(00)00646-9.

[24] S. SAMESHIMA, M. KAWAMINAMI, Y. HIRATA, Thermal Expansion of Rare-Earth-Doped Ceria Ceramics., J. Ceram. Soc. Jap. 110 (2002) 597–600. https://doi.org/10.2109/jcersj.110.597.

[25] T. Ivas, A. N. Grundy, E. Povoden-Karadeniz, L. J. Gaucklero, Phase diagram of CeO_2-CoO for nanosized powders., Calphad 36 (2012) 57– 64. https://doi.org/10.1016/j.calphad.2011.10.005.

[26] M. Chen, B. Hallstedt, A. N. Grundy, , L. J. Gauckler, CeO_2-CoO Phase Diagram., J. Am. Ceram Soc. 86 (2003) 1567–70.

[27] H. Okamoto, Cerium-Cobalt Binary Alloy Phase Diagram., ASM Alloy Phase Diagrams Center 2 (2007) 1047–1050.

[28] W. Zhuang, Z. Y. Qiao, S. Wei, J. Shen, Thermodynamic evaluation of the Cu-R (R: Ce, Pr, Nd, Sm) binary systems., J. Phase Eq. 17 (1996) 508–521. https://doi.org/10.1007/BF02665998.

[29] P. Knauth, G. Schwitzgebel, A. Tschöpe, S. Villain, Emf Measurements on Nanocrystalline Copper-Doped Ceria., J. Solid State Chem. 140 (1998) 295–299. https://doi.org/10.1006/jssc.1998.7890.

[30] X. Guo, R. Zhou, Identification of the nano/micro structure of CeO_2(rod) and the essential role of interfacial copper-ceria interaction in CuCe(rod) for selective oxidation of CO in H_2-rich streams., J. Power Sources 361 (2017) 39–53. https://doi.org/10.1016/j.jpowsour.2017.06.064.

[31] P. Duran, M. Gonzalez, C. Moure, J. R. Jurado, C. Pascual, A new tentative phase equilibrium diagram for the ZrO_2-CeO_2 system in air., J. Mater. Sci. 25 (1990) 5001–5006. https://doi.org/10.1007/BF00580121.

[32] K. Du, C.-H. Kim, A. H. Heuer, Structural Evolution and Electrical Properties of Sc_2O_3-Stabilized ZrO_2 Aged at 850˚C in Air and Wet-Forming Gas Ambients, J. Am. Ceram Soc. 91 (2008) 1626-1633. https://doi.org/10.1111/j.1551-2916.2007.02138.x.

[33] D. S. Lee, W. S. Kim, S. H. Choi, J. Kim, H. W. Lee, J. H. Lee, Characterization of ZrO_2 co-doped with Sc_2O_3 and CeO_2 electrolyte for the application of intermediate temperature SOFCs., Solid State Ionics 176, (2005) 33-39. https://doi.org/10.1016/j.ssi.2004.07.013.

[34] J. Marrero-Jerez, A. Murugan, I. S. Metcalfe, P. Núñez, TPR-TPD-TPO studies on CGO/NiO and CGO/CuO ceramics obtained from freeze- dried precursors., Ceram. Int. 40 (2014) 15175–15182. https://doi.org/10.1016/j.ceramint.2014.06.132.

[35] A. Pintar, J. Batista, S. Hocevarz, TPR, TPO, and TPD examinations of $Cu_{0.15}Ce_{0.85}O_{2-y}$ mixed oxides prepared by co-precipitation, by the sol-gel peroxide route, and by citric acid-assisted synthesis., J. Colloid Interface Sci. 285 (2005) 218–231. https://doi.org/10.1016/j.jcis.2004.11.049.

[36] L. Kundakovic, M. Flytzani-Stephanopoulos, Cu- and Ag-Modified Cerium Oxide Catalysts for Methane Oxidation., J. Catal. 179 (1998) 203–221. https://doi.org/10.1006/jcat.1998.2213.

[37] C.-W. Tang, C.-B. Wang, S.-H. Chien, Characterization of cobalt oxides studied by FT-IR, Raman, TPR and TG-MS., Thermochimica Acta 473 (2008) 68–73.[38] P. Arnoldy, J. A. Moulijn, Temperature-programmed reduction of $CoOAl_2O_3$ catalysts., J. Catal. 93 (1985) 38–54. https://doi.org/10.1016/j.tca.2008.04.015.

[39] H. C. Yao, Y. F. Y. Yao, Ceria in automotive exhaust catalysts: I. Oxygen storage., J. Catal. 86 (1984) 254–265. https://doi.org/10.1016/0021-9517(84)90371-3.

[40] B. Wang, J. Zhu, Z. Lin, A theoretical framework for multiphysics modeling of methane fueled solid oxide fuel cell and analysis of low steam methane reforming kinetics., Appl. Energ. 176 (2016) 1–11. https://doi.org/10.1016/j.apenergy.2016.05.049.

[41] K. Ukai, Y. Mizutani, Y. Kume, O. Y. H. Yokokawa, S. C. Singhal, Solid Oxide Fuel Cells, vol. VII., Electrochem. Soc., Pennington, NJ, 2001.

[42] J. Liu, S. A. Barnet, Operation of anode-supported solid oxide fuel cells on methane and natural gas., Solid State Ionics 158 (2003) 11–16. https://doi.org/10.1016/S0167-2738(02)00769-5.

[43] T. Ramos, J. Hjelm, M. Mogensen, Towards Quantification of Relations Between Electrode Polarisation and Microstructure., J. Electrochem. Soc. 158 (2011) B814–B824. https://doi.org/10.1149/1.3587113.

[44] T. Ramos, K. Thydén, M. Mogensen, Electrochemical Characterisation of Ni/(Sc)YSZ Electrodes., ECS Transac. 28 (2010) 123–139. https://doi.org/10.1149/1.3495837.

[45] A. Hagen, G. B. Johnson, P. Hjalmarsson, Electrochemical evaluation of sulfur poisoning in a methane-fuelled solid oxide fuel cell: Effect of current density and sulfur concentration., J. Power Sources 272 (2014) 776–785. https://doi.org/10.1016/j.jpowsour.2014.08.125.

[46] S. Park, R. Craciun, J. M. Vohs, R. J. Gorte, Direct Oxidation of Hydrocarbons in a Solid Oxide Fuel Cell I. Methane Oxidation., J. Electrochem. Soc. 146 (1999) 3603–3605. https://doi.org/10.1149/1.1392521.

[47] S. Park, R. J. Gorte, J. M. Vohs, Applications of heterogeneous catalysis in the direct oxidation of hydrocarbons in a solid-oxide fuel cell., Appl. Catal. A: Gen. 200 (2000) 55–61. https://doi.org/10.1016/S0926-860X(00)00650-5.

[48] K. Zhao, B.-H. Kim, Y. Du, Q. Xu, B.-G. Ahn, Ceria catalyst for inert- substrate-supported tubular solid oxide fuel cells running on methane fuel., J. Power Sources 314 (2016) 10–17. https://doi.org/10.1016/j.jpowsour.2016.02.079.

[49] W. J. S. Schmid, R. Hausbrand, Cobalt oxide thin film low pressure metal-organic chemical vapor deposition., Thin Solid Films 567 (2014) 8–13. https://doi.org/10.1016/j.tsf.2014.07.029.

[50] L. E. Gómez, J. F. Múnera, B. M. Sollier, E. E. Miró, A. V. Boix, Raman in situ characterization of the species present in Co/CeO_2 and Co/ZrO_2 catalysts during the COPrOx reaction., Int. J. Hydrogen Energ. 41 (2016) 4993–5002. https://doi.org/10.1016/j.ijhydene.2016.01.099.

[51] G. Balakrishnan, C. M. Raghavan, C. Ghosh, R. Divakar, E. Mohandas, J. I. Song, S. I. Bae, T. G. Kim, X-ray diffraction, Raman and photoluminescence studies of nanocrystalline cerium oxide thin films., Ceram. Int. 39 (2013) 8327–8333. https://doi.org/10.1016/j.ceramint.2013.03.103.

[52] A. Khana, C. Jiménez, O. Chaix-Pluchery, H. Roussel, J. L. Deschanvres, In-situ Raman spectroscopy and X-ray diffraction studies of the structural transformations leading to the $SrCu_2O_2$ phase from strontium-copper oxide thin films deposited by metalorganic chemical vapor deposition., Thin Solid Films 541 (2013) 136–141. https://doi.org/10.1016/j.tsf.2012.10.133.

[53] K. S. Rao, A. K. Chaudhary, F. Yehya, Investigation of solid carbon blacks using pulsed photoacoustic and double resonant Raman spectroscopy for the identification of trinitrotoluene., l 231 (2016) 830–836. https://doi.org/10.1016/j.snb.2016.03.052.

[54] B. M. Reddy, A. Khan, Y. Yamada, T. Kobayashi, S. Loridant, J.-C. Volta, Structural characterization of CeO_2-MO_2 (M = Si^{4+}, Ti^{4+}, and Zr^{4+}) mixed oxides by Raman spectroscopy, x-ray photoelectron spectroscopy, and other techniques., Journal of Physical Chemistry B 107 (2003) 11475–11484. https://doi.org/10.1016/10.1021/jp0358376.

[55] E. O. Jardim, S. Rico-Francés, F. Coloma, J. A. Anderson, E. V. Ramos- Fernandez, J. Silvestre-Alberoa, A. Sepúlveda-Escribano, Preferential oxidation of CO in excess of H_2 on Pt/CeO_2-Nb_2O_5 catalysts., Appl. Catal. A: Gen. 492 (2015) 201–211. https://doi.org/10.1016/j.apcata.2014.12.032.

[56] T. R. Reina, S. Ivanova, O. H. Laguna, M. A. Centeno, J. A. Odriozola, WGS and CO-PrOx reactions using gold promoted copper-ceria catalysts: “Bulk CuO CeO_2 vs. CuO CeO_2/Al_2O_3 with low mixed oxide content”., Appl. Catal. B: Envi. 197 (2016) 62–72. https://doi.org/10.1016/j.apcatb.2016.03.022.

[57] K. Singh, K. Kumar, S. Srivastava, A. Chowdhury, Effect of rare-earth doping in CeO_2 matrix: Correlations with structure, catalytic and visible light photocatalytic properties. Ceramics Int. 43, (2017) 17041-17047. https://doi.org/10.1016/j.ceramint.2017.09.116.

[58] J. Llorca, P. R. D. L. Piscina, J.-A. Dalmon, N. Homs, Transformation of Co_3O_4 during ethanol steam reforming. Activation process for hydrogen production., Chem. Mater. 16 (2004) 3573–3578. https://doi.org/10.1021/cm049311p.

[59] V. G. Hadjiev, M. N. Iliev, I. V. Vergilov, The Raman spectra of Co_3O_4., Journal of Physics C: Solid State Physics 21 (1988) L199–L201. https://doi.org/10.1088/0022-3719/21/7/007.

[60] G. J. Saunders, J. Preece, K. Kendall, Formulating liquid hydrocarbon fuels for SOFCs., J. Power Sources 131 (2004) 23–26. https://doi.org/10.1016/j.jpowsour.2004.01.040.

[61] N. K. Renuka, N. Harsha, T. Divya, Supercharged ceria quantum dots with exceptionally high oxygen intermediate action., RSC Advances 5 (2015) 38837–38841. https://doi.org/10.1039/c5ra01161b.